applied sciences

MDPI

Article

Model Test and Numerical Simulation for Tunnel Leakage-Induced Seepage Erosion in Different Strata

Qihao Sun [1,2], Wouter De Corte [2,*], Xian Liu [1,3] and Luc Taerwe [1,2]

[1] College of Civil Engineering, Tongji University,1239 Siping Road, Shanghai 200092, China; 1732381-sqh@tongji.edu.cn (Q.S.); xian.liu@tongji.edu.cn (X.L.); luc.taerwe@ugent.be (L.T.)
[2] Department of Structural Engineering and Building Materials, Ghent University, Technologiepark Zwijnaarde 60, 9052 Ghent, Belgium
[3] State Key Laboratory for Hazard Reduction in Civil Engineering, Tongji University, Shanghai 200092, China
* Correspondence: wouter.decorte@ugent.be

Abstract: Leakage in underground structures, especially tunnels, may cause seepage erosion in the surrounding soil, which in turn leads to ground subsidence, posing a great threat to urban safety. The current literature mainly focuses on seepage erosion in the sand but lacks a systematic study on the development process of seepage erosion induced by tunnel leakage in different strata. To investigate the different seepage erosion modes induced by tunnel leakage in different stratum types, a series of reduced-scale model tests were carried out. A coupled fluid–solid numerical model was further established to analyze the fine-scale characteristics of different seepage erosion modes. The results show that (1) the soil seepage erosion modes can be divided into three categories: no soil cave, unstable soil cave, and stable soil cave; (2) the adopted coupled fluid–solid numerical model based on DEM, which takes into account the degradation of clay during seepage erosion, can effectively simulate the erosion process of soil with different seepage erosion modes; (3) the phenomena of the three erosion modes are different in the process of erosion development; and (4) the micro-mechanisms of the three seepage erosion modes are different, which are manifested in the erosion range, soil arching effect, and displacement.

Keywords: tunnel leakage; seepage erosion; coupled fluid–solid model; model test; soil arching effect

check for updates

Citation: Sun, Q.; De Corte, W.; Liu, X.; Taerwe, L. Model Test and Numerical Simulation for Tunnel Leakage-Induced Seepage Erosion in Different Strata. *Appl. Sci.* **2024**, *14*, 3908. https://doi.org/10.3390/app14093908

Academic Editor: Tiago Miranda

Received: 27 March 2024
Revised: 28 April 2024
Accepted: 30 April 2024
Published: 3 May 2024

Copyright: © 2024 by the authors. Licensee MDPI, Basel, Switzerland. This article is an open access article distributed under the terms and conditions of the Creative Commons Attribution (CC BY) license (https://creativecommons.org/licenses/by/4.0/).

1. Introduction

Hazards such as leakage [1] or earthquakes [2,3] in underground structures may induce severe consequences, including surface subsidence, structure damage, and even casualties, which seriously threaten urban safety. Among them, leakage of underground pipelines and subway tunnels is the major cause of induced ground subsidence [4–7]. The reason for this is that when leakage occurs in underground structures such as tunnels, the surrounding soil continues rushing into tunnels due to seepage forces, triggering catastrophic consequences such as ground subsidence. Recent research indicates the potential of deep learning techniques in identifying damages within tunnel structures [8] and enhancing the resilience of underground structures by structural health monitoring in this field [9,10]. However, to prevent the hazards, an investigation into the mechanism is also necessary.

The essence of the problem of tunnel leakage-induced disasters is seepage erosion of the strata. To investigate the disasters caused by water leakage in tunnels, research has been conducted through model tests. Zheng, et al. [11] conducted a reduced-scale model test to investigate the settlement pattern of strata generated by soil erosion after tunnel leakage and proposed a simplified calculation formula for settlement. Guo, et al. [12] investigated the effects of four parameters, including soil particle size, pipe crack dimension, water height, and soil depth, on the erosion process of strata around a cracked sewage pipe. Tang, et al. [13] selected three kinds of quartz sands with different particle sizes and carried out

an experimental study on the erosion development process of the strata outside a damaged sewage pipe.

In addition to the reduced-scale model tests, researchers also adopted numerical simulation methods to explore the erosion development process of the external strata after leakage in underground structures. Due to the characteristics of soil as a typical discontinuous granular material, the discrete element method (DEM) is an effective numerical simulation method in this field. Different calculation methods of fluid are coupled with DEM to realize the coupled fluid–solid analysis of the seepage erosion process. Zhang, et al. [14] simulated the erosion process of soil caused by periodic water level changes using a CFD-DEM model. Long and Tan [15] adopted a coupled FDM-DEM method to simulate the erosion in water-rich sands due to tunnel leakage, and further analyzed the existence of the soil arching effect in this phenomenon. Zhang, et al. [16] dealt with the simulation of the tunnel leakage issue by first calculating the distribution of water pressure around the tunnel when leakage occurs using FEM, and then applying the hydraulic forces to the DEM model, to analyze the erosion of the strata induced by the tunnel leakage.

From the above discussion, it can be seen that there are already some studies on the seepage erosion problem induced by tunnel leakage. However, the existing research mainly focuses on seepage erosion that occurs in sandy soil strata, and less on the other types of soil such as silt, clay, etc. The seepage erosion modes in different strata have not yet been clarified. Actually, in many accidents induced by tunnel leakage, the erosion and damage modes are different, but the mechanisms and development processes have not been systematically investigated. Therefore, it is necessary to carry out research on the seepage erosion mode of tunnel leakage in different soil types.

To investigate the damage modes and mechanisms of seepage erosion induced by tunnel leakage in different types of strata, a series of tests on soil seepage erosion was designed and carried out. From this, the differences in the process of seepage erosion induced by tunnel leakage in different soils were investigated. Furthermore, through establishing a coupled fluid–solid simulation model, the mechanisms that generate different erosion damage modes are explored. This study is intended to provide a reference for the prevention and control of seepage-induced disasters in underground structures in the future.

2. Model Test

2.1. Test Design

A reduced scale model test was carried out based on recorded leakage accidents that occurred at the entrance and exit of shield tunnels. The test was carried out in a model box with a scale factor of 50:1. The model box is shown in Figure 1a, with dimensions of 1400 mm × 400 mm × 1000 mm. The colored sand layers were used to visualize the displacement of the strata. The model box consists of a soil box in the center and two water tanks on both sides to provide water for the tunnel leakage and to control the water level. The tunnel was buried in the soil box, which was separated from the two water tanks by permeable plates, which meet the requirements of water permeability and soil impermeability. Overflow outlets were set on both outsides of the tanks. Water was continuously refilled into the tanks during the test. Due to the presence of the overflow outlets, the water level was constant as it would flow out once it exceeded the height of the overflow outlets. In addition to this, the interior of the model box panels was coated with Vaseline to minimize friction between the soil and the boundary.

A leakage may occur at different locations within the tunnel. In this research, leakage at the tunnel top is used as an example to compare the phenomenon of seepage erosion in different strata. During the test, an opening was made at the top of the tunnel in advance and sealed with a rubber plug. Then, at the beginning of the test, the plug was removed to trigger water and sand inrush, as shown in Figure 1b. The size of the openings is 2 cm × 2 cm, which is large enough to ensure that the water and sand rush in continuously [11] since the focus of the study lies primarily on investigating the differences

in seepage erosion among different strata. Therefore, factors such as the shape or dimension of the opening were not explicitly considered, which will be investigated in future work.

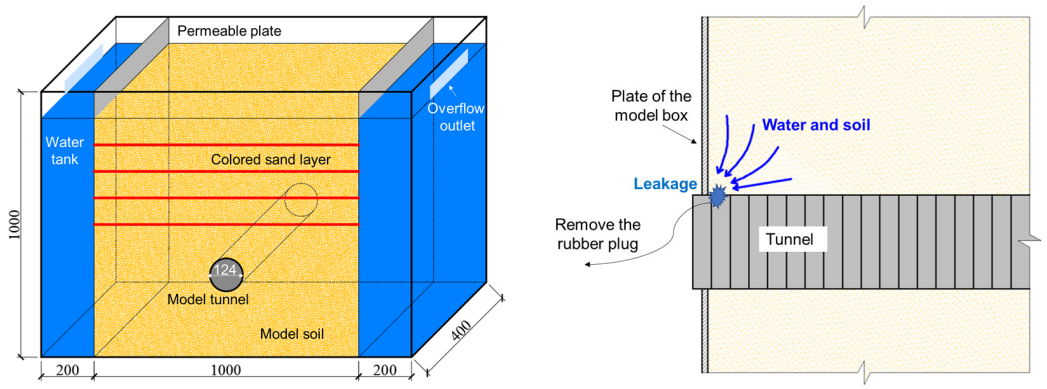

Figure 1. Model test device: (**a**) model test box (unit: mm); (**b**) illustration of the test process.

In order to study the difference in seepage erosion caused by tunnel leakage in different soil types, different proportions of sand and clay were mixed to obtain different model soils. These soils exhibit stability in their properties, with obvious differences in their physical–mechanical parameters. The raw material of sand is quartz sand, which is stable and free of impurities. In order to ensure that seepage erosion can occur in the soil, the sand used in the tests has the following characteristics: d_{60} = 1 mm, d_{10} = 0.1 mm. The grading curve is shown in Figure 2. The clay material was selected from natural clay with a cohesion of 20.4 kPa, a friction angle of 18.5°, and a permeability coefficient of 1.26×10^{-7} cm/s. Clay percentages of 0%, 5%, 10%, and 20% were added to the quartz sand to make four types of soil (A, B, C, and D). The physical and mechanical parameters of the mixed soil with different mixing ratios are shown in Table 1.

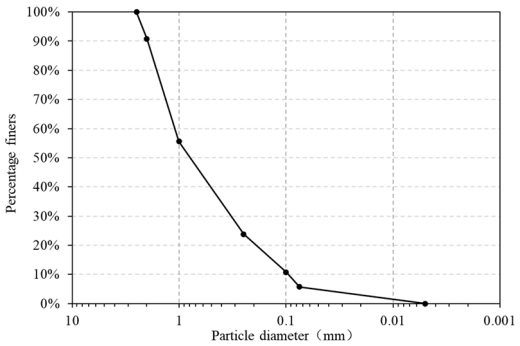

Figure 2. Particle size distribution curve of sand.

Table 1. Parameters of model soil.

Soil Type	Content of Clay (%)	Unit Weight (kN/m^3)	Cohesion (kPa)	Friction Angle (°)	Permeability Coefficient (m/s)
A	0	14.7	0	40.17	2.21×10^{-5}
B	5	15.1	1.81	35.56	1.33×10^{-6}
C	10	15.4	2.88	35.87	8.04×10^{-7}
D	20	15.8	4.28	34.16	6.45×10^{-7}

The seepage process involves the interaction of water and soil particles at the same time, which belongs to the fluid–solid coupling problem. Liu, et al. [17] pointed out through

tests that the permeability coefficient of soil is a key parameter affecting the seepage erosion process. When normal gravity conditions are used in the test, the similarity of acceleration $\lambda_a = 1$, the similarity of density ratio $\lambda_\rho = 1$, and the similarity of geometric length $\lambda_L = 50$. Based on the above three basic physical variables, it can be deduced through the dimensional analysis that the similarity of the permeability coefficient $\lambda_p = \sqrt{50}$. Therefore, the four types of soil correspond to different types of soil prototypes based on the similar relationship of the permeability coefficients. The prototype of soil A is sand, and the prototype permeability coefficient is 1.56×10^{-4} m/s. The prototype of soil B is silt, and the prototype permeability coefficient is 9.40×10^{-6} m/s. The prototypes of soil C and D are silty clay or clay with a small permeability coefficient. The permeability coefficients of the prototypes are 5.69×10^{-6} m/s and 4.56×10^{-6} m/s.

Gypsum is used as the material for the reduced-scale model tunnel. The dimensions of the model tunnel adhere to a scale factor of 50:1 when compared with the prototype. Also, the compressive strength of gypsum material in the model tunnel is 1.1 MPa, which meets the similarity ratio of compressive strength, which is 55 MPa in the actual subway tunnel. The model tunnel is shown in Figure 3.

Figure 3. Model tunnel.

2.2. Test Results

During the test, the phenomena of tunnel leakage-induced seepage erosion in different strata differed significantly, and, in order to facilitate the comparison and analysis, the phenomena were processed by the Particle Image Velocimetry (PIV) technique [18]. The phenomena of erosion in soil A are shown in Figures 4 and 5, where the green arrows in Figure 4 indicate the direction of displacement, and Figure 5 shows the velocity distribution field. The erosion process in soil A can be summarized as follows. (1) Stage 1: after leakage occurred at the top of the tunnel, the water and soil mixture rapidly poured through the opening. (2) Stage 2: an apparent displacement appeared in the soil above the tunnel, and developed upward to the soil top. (3) Stage 3: a slip surface appeared in the soil, and the soil top within the slip surface subsided. From the above observation, it can be seen that the soil loss in soil type A was continuous during the whole process.

The strata response in soil B is shown in Figures 6 and 7. The process can be summarized into four stages. (1) Stage 1: after leakage initiates, soil and water start to rush into the tunnel, and seepage erosion of the surrounding soil starts. (2) Stage 2: due to the loss of soil and water at the top of the tunnel, an initial soil cave was formed above the tunnel, which temporarily remained stable. (3) Stage 3: the initial soil cave destabilized, and the soil above the cave collapsed rapidly. Subsequently, a secondary soil cave was formed and stabilized again. (4) Stage 4: the secondary soil cave destabilized and the soil above the cave, including the soil surface, subsided instantly and impacted the tunnel.

In the test of soil B, the phenomena of the soil cave were observed after the erosion occurred. The surface was stable during the development of the erosion. However, the soil cave was unstable and continued to develop. Eventually, when the soil cave reached a critical height, the soil surface destabilized and fell.

Regarding the discussion of soils C and D, it was observed that in the test, soil C showed the same phenomena as soil D. Therefore, soil C is taken as an example for the discussion of soils C and D.

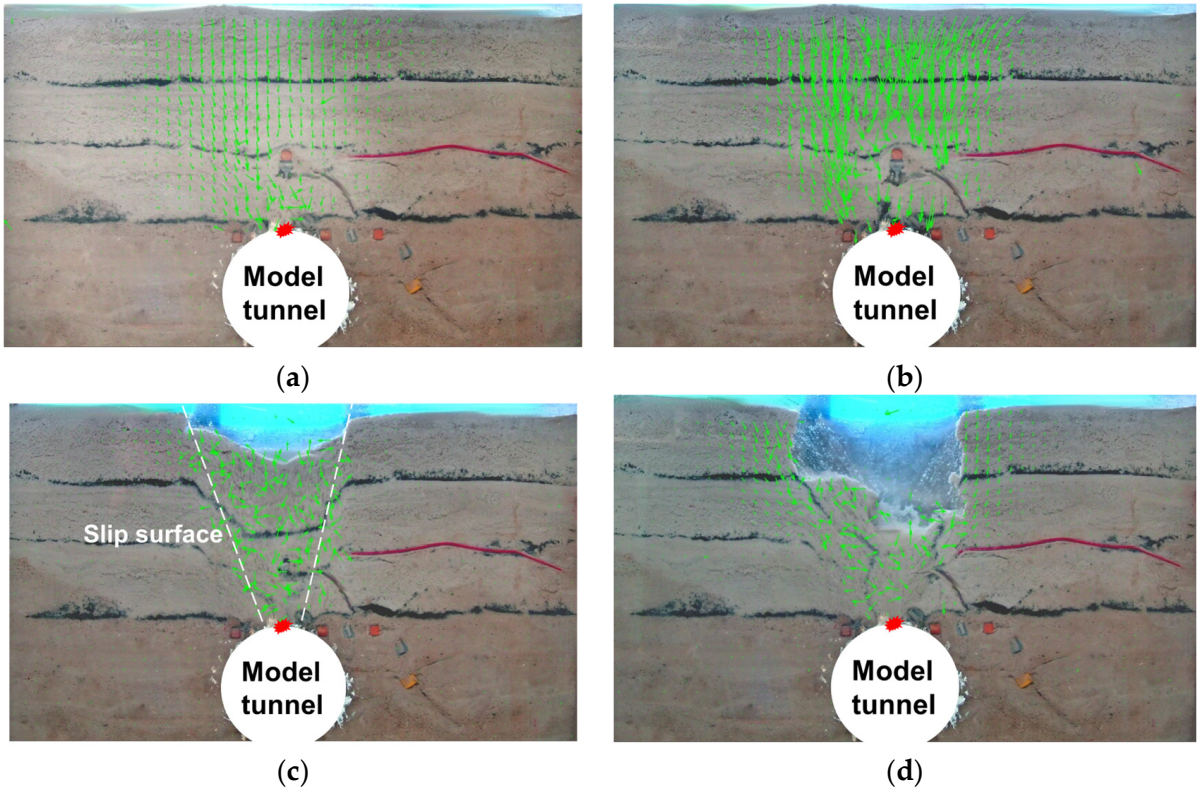

Figure 4. Displacement of soil A: (**a**) leakage at the tunnel top; (**b**) soil displacement; (**c**) slip surfaces; (**d**) subsidence within the slip surface.

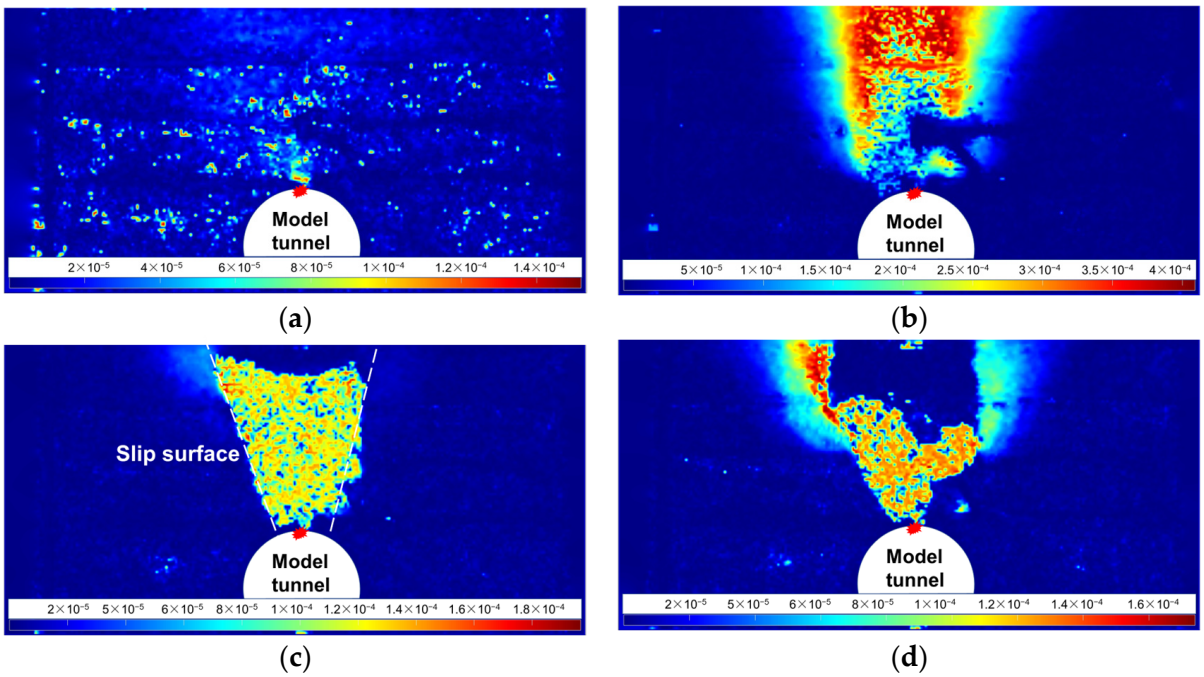

Figure 5. Velocity distribution of soil A (m/s): (**a**) leakage at the tunnel top; (**b**) soil displacement; (**c**) shear slip surfaces; (**d**) subsidence within the slip surfaces.

Its strata response is shown in Figure 8. It can be seen that after the tunnel leakage, a soil cave appeared on the top of the tunnel, and a small amount of soil flowed out. But, after

120 min, the soil cave remained stable without any further development, which indicated that the stratum stabilized itself spontaneously.

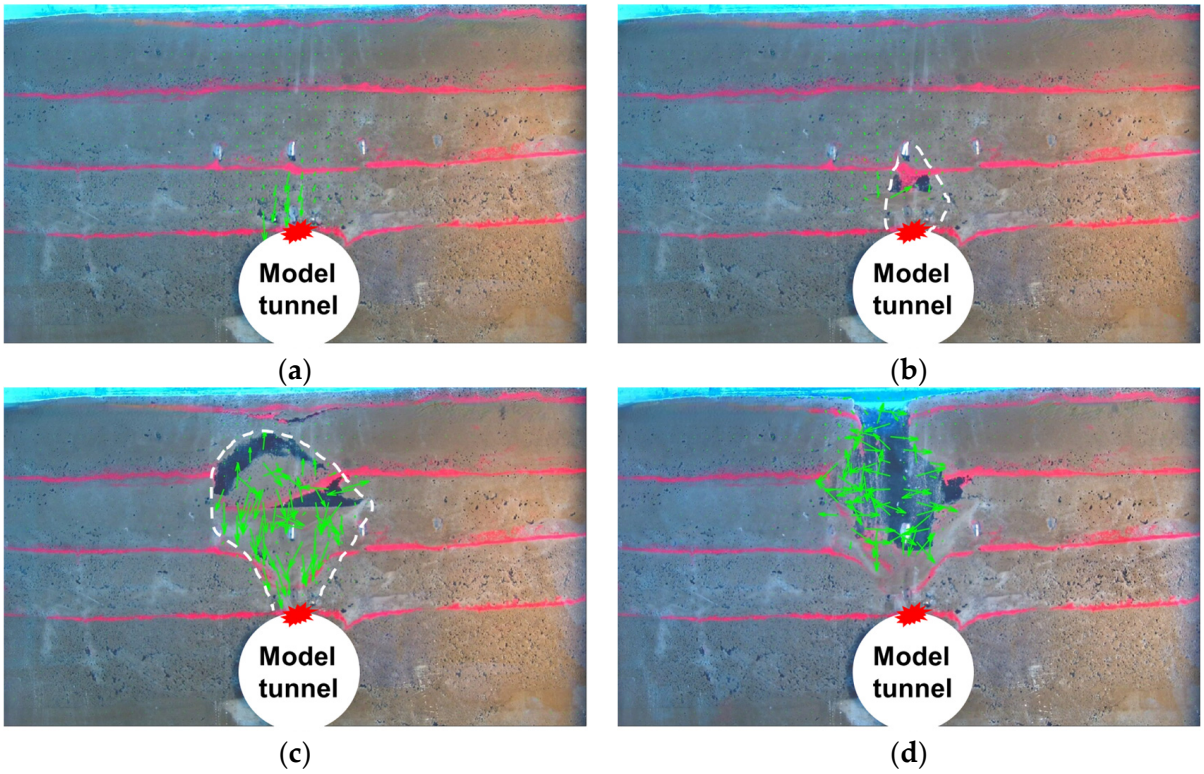

Figure 6. Displacement of soil B: (**a**) leakage at the tunnel top; (**b**) initial soil cave; (**c**) secondary soil cave; (**d**) surface subsidence.

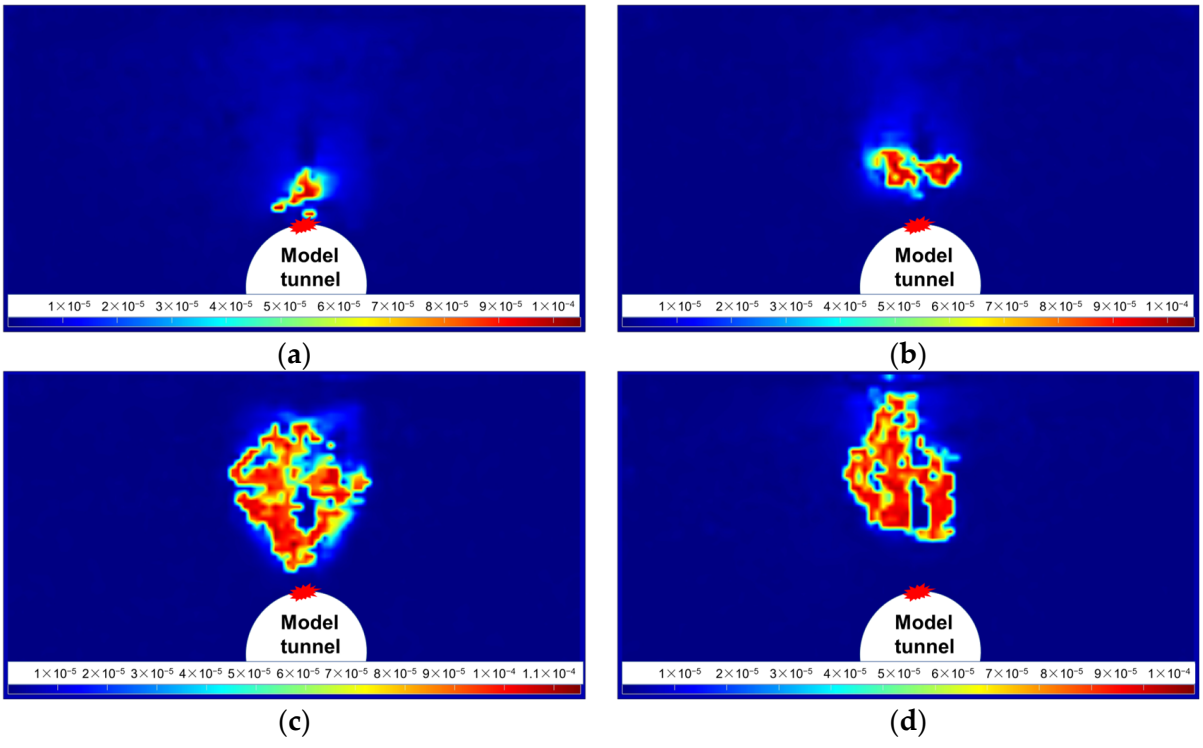

Figure 7. Velocity distribution of soil B (m/s): (**a**) leakage at the tunnel top; (**b**) initial soil cave; (**c**) secondary soil cave; (**d**) surface subsidence.

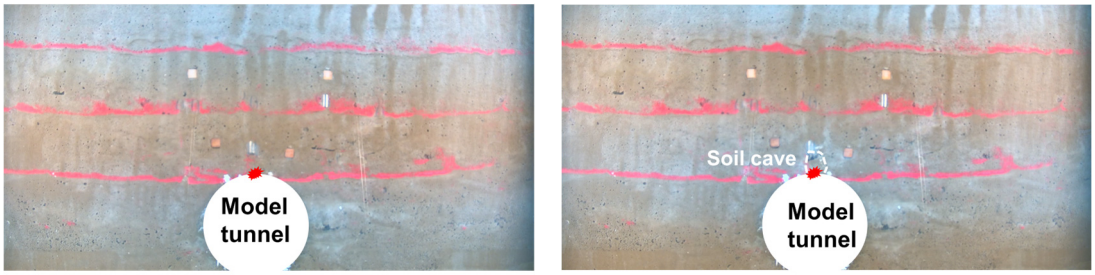

(**a**) (**b**)

Figure 8. Phenomena of soil C: (**a**) leakage at the tunnel top; (**b**) soil remains stable after 120 min.

It can be summarized that the seepage erosion in the four different types of soil showed three completely different development processes:

(1) For soil A, a slip surface developed rapidly after the tunnel leakage, which extended to the soil top and caused the surface to subside. No soil cave was observed during the whole process. In what follows, soil A is referred to as the no soil cave (NSC) soil.

(2) For soil B, after the tunnel leakage, soil caves were observed. However, the soil caves were unstable and continued to destabilize and reappear with seepage erosion. The soil surface remained stable until the soil cave reached a critical height. In what follows, soil B is referred to as the unstable soil cave (USC) soil.

(3) For soil C and D, after the tunnel leakage, a stable soil arch was observed near the leakage point and the soil stabilized spontaneously. In what follows, soil C is referred to as the stable soil cave (SSC) soil.

For other soil with a clay addition higher than 10%, an experimental study by Liu et al. [17] has provided compelling evidence of the correlation between clay content and the stability of the soil. Liu conducted a series of seepage experiments specifically targeting clay content, demonstrating that as the clay content increases, the soil exhibits greater stability and resistance against seepage erosion. Therefore, considering Liu's findings, it is reasonable to classify soil C, D, and soil with a clay addition higher than 10% as stable soil cave soil.

3. Coupled Fluid–Solid Simulation Model

3.1. Description of the Coupled Fluid–Solid Model

When simulating seepage erosion, consideration was given to the characteristics of the mixed soil composed of sand and clay. For soil predominantly consisting of sand, the erosion process involves the detachment, transportation, and clogging of particles [19–23], driven by hydraulic forces. These phenomena were simulated with the coupled fluid–solid model, using FDM to calculate fluid dynamics and DEM to simulate soil particles. However, with the addition of clay, they adhere to the surface of sand particles, affecting the contact behavior between sand particles. These clay particles are lost during seepage erosion. Degradation caused by seepage-induced erosion of clay is considered and addressed in Section 3.2.

Since only the damage phenomena can be obtained from the model test and the differences in the mechanism of erosion cannot be analyzed in depth, the seepage erosion in different strata is further analyzed by numerical simulation. From the test results, it can be seen that the seepage erosion caused by tunnel leakage is mainly concentrated in the vertical plane perpendicular to the tunnel axis where the seepage point is located, so a two-dimensional coupled flow–solid model is established for simulation. FDM and DEM are coupled in the numerical model, in which the soil is simulated by DEM and fluid is simulated by FDM. The forces applied to the soil particles in the flow field meet Equation (1):

$$\frac{\partial \vec{u}}{\partial t} = \frac{\vec{f}_{mech} + \vec{f}_{fluid}}{m} + \vec{g} \quad (1)$$

where $\vec{u}$ is the particle velocity, m is the particle mass, $\vec{f}_{fluid}$ is the hydraulic force applied on the particle, $\vec{f}_{mech}$ is the sum of the external forces acting on the particle (externally exerted force and contact force between the particles), and $\vec{g}$ is the acceleration of gravity.

The force $\vec{f}_{fluid}$ acting on the particles is mainly composed of the drag force generated by the fluid [24], which can be calculated according to the following equation:

$$f_{drag} = V_i \gamma_w i \tag{2}$$

where V_i is the particle volume, γ_w is the unit weight of water, and i is the hydraulic gradient.

To realize the bidirectional coupling between fluid and soil, the influence of the soil on the flow field is reflected through the change of permeability coefficient. For granular materials, the permeability coefficient can be obtained by converting the porosity, which is based on the Kozeny–Carman equation [25]:

$$k = \frac{1}{C_s S_s^2 T^2} \frac{\gamma_w}{\mu} \frac{e^3}{1+e} \tag{3}$$

Here, C_s is the shape factor of the granular material, S_s is the surface area per unit volume of the soil, T is the tortuosity factor, μ is the dynamic viscosity, and e is the void ratio.

To realize the bidirectional coupling calculation, the DEM and FDM joint calculation method is adopted in the model, as shown in Figure 9. The DEM analysis was performed with the commercial DEM software PFC 5.0 [26]. The FDM calculation was performed with the commercial FDM software FLAC 5.01 [27]. The influence of the flow field on particle behavior is simulated by calculating seepage forces in the FDM model. These seepage forces are then applied to the particles in the DEM model to simulate the effect of the flow field on particles. Conversely, the impact of particles on the flow field is achieved by altering the permeability coefficient in the FDM model. Soil particles undergo movement, resulting in changes in their porosity, which is then converted into a permeability coefficient. The corresponding adjustment of the permeability coefficient in the FDM model enables recalculating the flow field to reflect the influence of particles on the flow field. This method has been validated in the literature. For instance, Long and Tan [15] adopted a coupled FLAC-PFC model to simulate erosion in water-rich sands due to tunnel leakage. They successfully simulated the displacement and loss of soil due to tunnel leakage by computing the flow field response with FLAC and the particle response with PFC. The overall calculation process is briefly described hereunder:

(1) The FDM software is used to establish the fluid analysis model and the DEM software is used to establish the soil model, respectively.

(2) The fluid mesh and node information are transferred to the DEM program and the corresponding fluid parameters are set.

(3) The flow field is calculated by the FDM software, and the calculated pressure field distribution and velocity are sent to the DEM software.

(4) The fluid field is read by the DEM software, and the hydraulic forces are applied to the particles. Then, the DEM model is calculated. In this erosion scheme, the driving forces include the gravity on the soil particles and the hydraulic force from fluid flow.

(5) After completing the calculation, the porosity of each fluid unit is read by the DEM software and converted into a permeability coefficient, which is returned to the FDM software to update the parameters of the flow field.

(6) The condition of termination in this model is the number of calculation steps. Calculation steps (3) to (5) are repeated until the condition for termination is reached.

In the FDM calculation, the time step is determined using the von Neumann stability method [28], which is commonly used to determine the time step to ensure numerical stability.

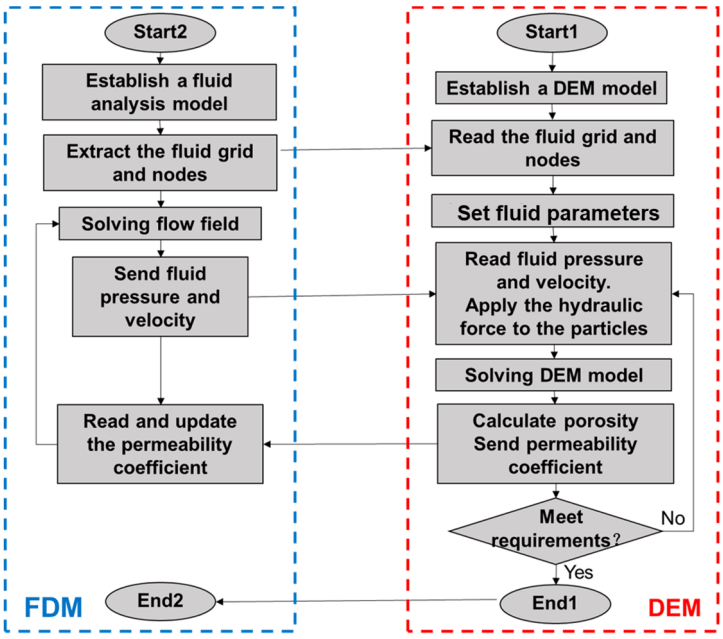

Figure 9. Fluid–solid coupling calculation process.

3.2. Seepage-Induced Erosion of Clay

Due to the extremely small diameter of clay particles, it is impossible to model clay particles in the actual size to reflect their mechanical properties in the DEM model. However, the presence of clay greatly affects the physical and mechanical properties of the soil, especially because the process of seepage erosion is also accompanied by the loss of clay. To solve the problem, clay degradation is considered within the coupled flow–solid model.

In the model test, to obtain soil samples with different properties, quartz sand was mixed with different proportions of clay. When seepage erosion occurs in the mixed soil, the clay that wraps the quartz sandy particles is lost, accompanied by the loss of fine sand particles. The erosion and degradation process of the mixed soil is shown in Figure 10. In the simulation, to reflect the process of clay erosion and degradation, the gradual loss of clay by the seepage forces is realized by decreasing the contact strength between discrete element particles [29,30].

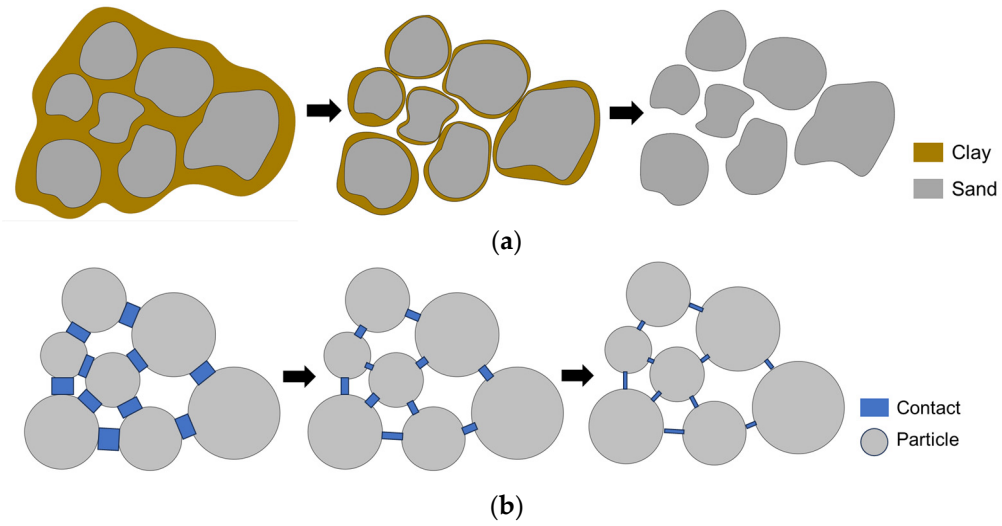

Figure 10. Schematic diagram of clay erosion degradation [29,30]: (**a**) erosion degradation of clay; (**b**) realization with DEM.

Loss of clay occurs when the hydraulic shear stress exceeds the critical shear stress of the clay; otherwise, no loss of clay mass occurs. The lost clay mass during seepage erosion can be calculated by Equation (4) [29,30].

$$m = \begin{cases} k_{er}(|\tau| - \tau_c)^b, if\ |\tau| > \tau_c \\ 0,\ otherwise \end{cases} \tag{4}$$

where m is the mass of lost soil per unit area and time ($kg/(m^2 \cdot s)$), b is an exponent. Hanson, et al. [31] compiled many tests conducted on the erosion of cohesive soils, such as open channel tests and streambed tests. Based on these tests, the coefficient b was suggested to be 1. k_{er} is the erosion rate, τ is the shear stress at the interface, and τ_c is the critical shear stress.

In DEM modeling, when simulating soils with clay addition, the contact model is usually chosen to be the linear contact bond model, while the contact model adopted in simulating sands is commonly the linear model [26]. The main difference between the two contact models is that tensile and shear bond strengths are considered in the linear contact bond model. Therefore, it is assumed that the shear and tensile bond strengths in the linear contact bond model come from the contribution of the added clay. When the clay is completely lost, the shear and tensile bond strengths are completely reduced to zero and the linear contact bond model degrades to the linear contact model.

Based on this assumption, the ratio of the reduction in the shear and tensile bond strengths to the original strength is equal to the ratio of the mass of clay lost to the mass of the original clay. Taking the tensile strength σ as an example, Equation (5) is satisfied:

$$\frac{\Delta\sigma}{\sigma} = \frac{\Delta m_{j_clay}}{m_{j_clay}} \tag{5}$$

where Δ denotes the amount of change in the corresponding physical quantity, σ is the tensile strength of the contact between the particles, and m_{j_clay} is the mass of clay attached to the surface of the particle j.

Based on this idea, the corresponding decay ratio of the contact bond strength is further determined. Assuming that the clay is uniformly distributed on the surface of all sand particles according to the surface area of the sand particles, all particles share a clay content equal to the proportion of the surface area of the particles themselves. Assuming that there are a total number of N particles and the total mass of clay is m_{clay}, then the mass of clay shared by the particle j (m_{j_clay}) can be calculated according to Equation (6).

$$m_{j_clay} = 4\pi R_j^2 \frac{m_{clay}}{\sum_{i=1}^{N} 4\pi R_i^2} \tag{6}$$

where R is the radius of the particle.

The mass of clay lost per unit area and per unit time is calculated by $k_{er}(|\tau| - \tau_c)^b$, multiplied by Δt and the surface area of particles of attached clay $4\pi R_j^2$, and the total mass of clay lost in the period is obtained, as shown in Equation (7):

$$\Delta m_{j_clay} = \Delta t k_{er}(|\tau| - \tau_c)^b 4\pi R_j^2 \tag{7}$$

Combining Equations (7) and (5), the deterioration formulas for contact bond strength can be obtained. Taking the tensile strength σ as an example, its decay strength after time Δt is as follows:

$$\Delta\sigma = \sigma \frac{\Delta m_{j_clay}}{m_{j_clay}} = \sigma \frac{\Delta t k_{er}(|\tau| - \tau_c)^b 4\pi R_j^2}{m_{j_clay}} \tag{8}$$

In the DEM model, computations based on the FDM are conducted on grids. Within each grid cell, a uniform distribution of seepage forces is assumed. Subsequently, the

shear forces acting on particles within each grid cell can be calculated, and it is determined whether these shear forces exceed the critical shear stress of the clay. If they surpass this threshold, Equation (6) is utilized to calculate the necessary reduction in contact strength, and, subsequently, the contact strength within the grid cell is adjusted accordingly.

In this method, the determination of erosion occurrence in the clay is based on whether the shear forces generated by seepage exceed the shear strength. Subsequent calculations are also predicated on this criterion. During the erosion process, particle velocities are directly proportional to the shear forces induced by seepage. Therefore, the criterion of seepage forces adequately represents the velocities associated with erosion phenomena, obviating the need for redundant consideration of velocity as a separate parameter.

3.3. Simulation Process and Parameters

In the DEM model, the contact between the soil particles is set as the linear contact bond model. The particle-to-particle bond breaks after reaching the bond strength and degrades into the linear contact model. Parameter calibration was carried out by shear tests, and the detailed parameters of the models corresponding to the three different soil types are shown in Table 2. It should be noted that the shear and tensile strength of the contacts in NSC is zero, so the linear contact bond model degrades to the linear contact model. The linear contact bond model for NSC was chosen but the contact strength is set to zero to make it consistent with the other two types of soil.

Table 2. Parameters of the model.

Component	Soil Type	NSC	USC	SSC
Contacts	Friction coefficient	0.9	0.8	0.8
	Normal stiffness (N/m)	5.0×10^7	10.0×10^7	10.0×10^7
	Shear stiffness (N/m)	2.5×10^7	5.0×10^7	5.0×10^7
	Tensile strength (force) (N)	0	36	40
	Shear strength (force) (N)	0	36	40
Particles	Particle density (kg/m^3)		2700	
	Damping		0.7	
	Porosity of soils		0.4	
Fluid	Density (kg/m^3)		1000	
	Fluid bulk modulus (Pa)		2.0×10^9	

From the tests, it was observed that the range of soil erosion where tunnel leakage was induced was smaller than the size of the model test box (1000 mm × 1000 mm). Therefore, to effectively utilize the computational resources, the size of the calculated soil model was decided based on the region of stratum displacement that occurred in the test. Considering the results of the model tests of the three different strata, the dimensions of the model are 800 mm in width and 660 mm in height. Based on the above considerations, the DEM model and the FDM model were established.

The FDM model is shown in Figure 11a. The elements were divided uniformly, the length of each element side was 20 mm, and the surrounding area of the tunnel was adjusted according to its shape. A total of 1320 FDM elements were generated. The water pressure boundary conditions were set according to the model tests. The tunnel opening was set as the outlet boundary. Therefore, the pressure boundary at the opening was set to zero. In addition, the pressure at the surface was set to zero. The other surface (i.e., the sides and bottom) was set as walls, and the pressure was set according to the actual water pressure distribution, as shown in Figure 11b.

The water pressure distribution in the numerical model is identical to the conditions of the physical model tests to ensure that the numerical simulation accurately replicates the results of the model tests. In the model tests, as illustrated in Figure 1a depicting the model box design, water supply to the soil originates from water tanks on both sides. Upon filling these tanks, the water pressure on both sides exhibits a gradient distribution under

gravity, increasing gradually from the water surface to the bottom. Due to the presence of permeable plates separating the soil from the water tanks, the water pressure at the sides of the soil matches the distribution of water pressure in the tanks, thus demonstrating the gradient change as shown in Figure 11b.

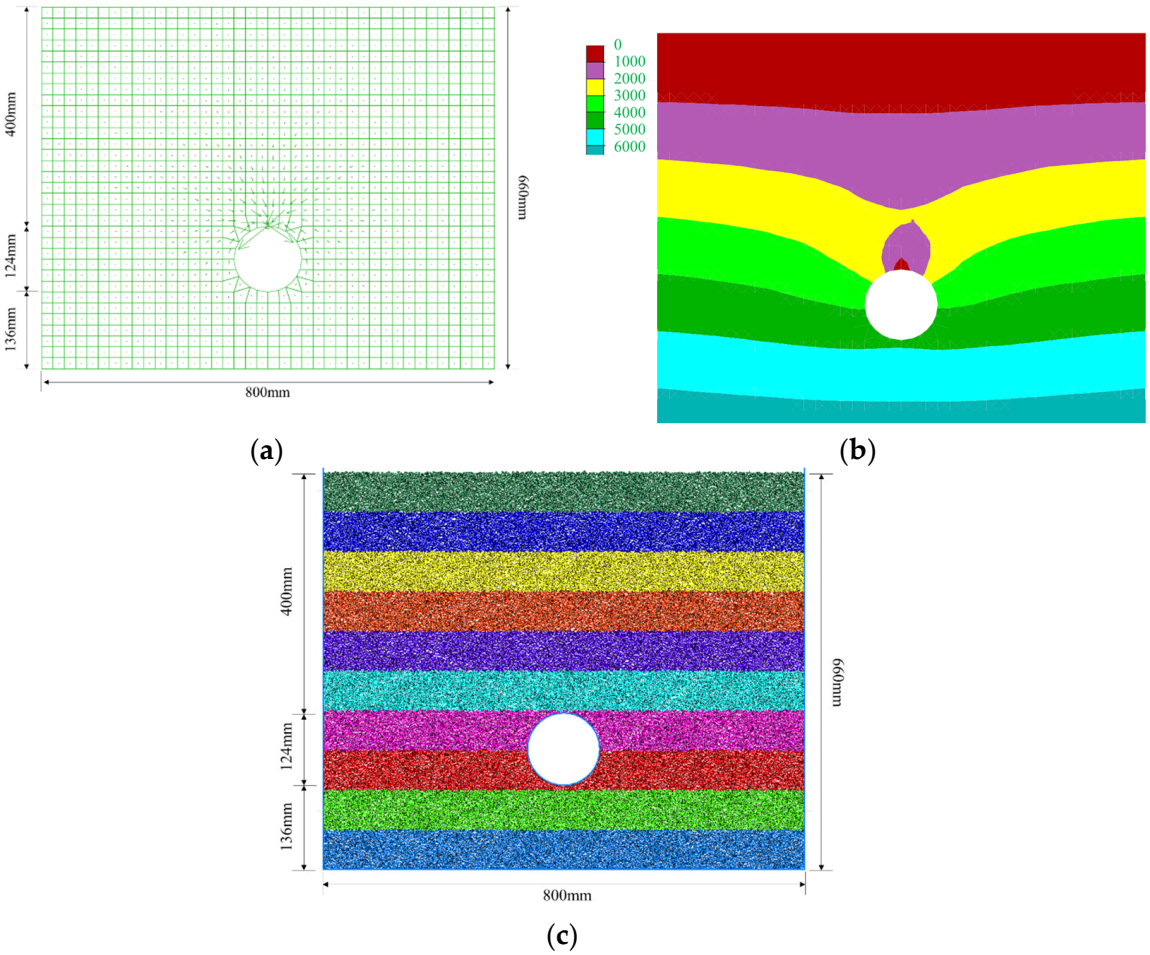

Figure 11. FDM and DEM model: (**a**) FDM model; (**b**) distribution of pressure (Pa); (**c**) DEM model.

If the DEM particles are modeled according to the actual particle size, the number of particles in the model is too large for effective computation. Therefore, it was considered to amplify the particles without affecting the properties of the soil. Deisman, et al. [32] proposed the following equation to describe the particle size effect:

$$RES = \left(\frac{L}{R_{min}}\right)\left(\frac{1}{1+\frac{R_{max}}{R_{min}}}\right) \quad (9)$$

where L is the length of the shortest side of the model, and R_{max} and R_{min} are the maximum and minimum particle diameters, respectively. When $RES \geq 10$, the size and number of particles in the model have only a small influence on the mechanical properties of the soil. Considering the model size and computational ability, the soil particles in the model were enlarged by a factor of 2.5. The shortest side of the model was taken as the diameter of the shield tunnel R = 124 mm, the maximum particle diameter of the enlarged model particles was 2.5 mm, and the minimum particle diameter was 0.25 mm. Then, RES in this model is 45, which meets the above requirements, and the enlarged particles should not influence the mechanical behavior of the soil. A rigid circular wall was used to simulate the tunnel. The way of triggering the water and sand inrush was consistent with the model test by deleting part of the wall at the corresponding position. Due to the enlargement of the

particles, the size of the tunnel opening was also enlarged. The size of the tunnel opening in the model test is 2 cm, and the size of the tunnel opening in the numerical simulation was enlarged to 5 cm. The model of the strata is shown in Figure 11c. The boundary conditions of the strata model refer to the test settings and are consistent with the tests. The walls of the model are fixed boundaries and impenetrable to particles. There is no friction between the particles and the wall, simulating the smooth boundary conditions in the tests. Based on the results of sensitivity analyses on the timestep [33], the time step of the DEM was set to be 1.0×10^{-6} s.

3.4. Model Validation

The numerical simulation results of the NSC soil are shown in Figure 12. As can be seen from the figure, the numerical simulation reproduces the key phenomena observed in the test. After the tunnel leakage, the soil particles were lost continuously with the seepage erosion, and no obvious soil cave phenomenon appeared in the process of erosion development.

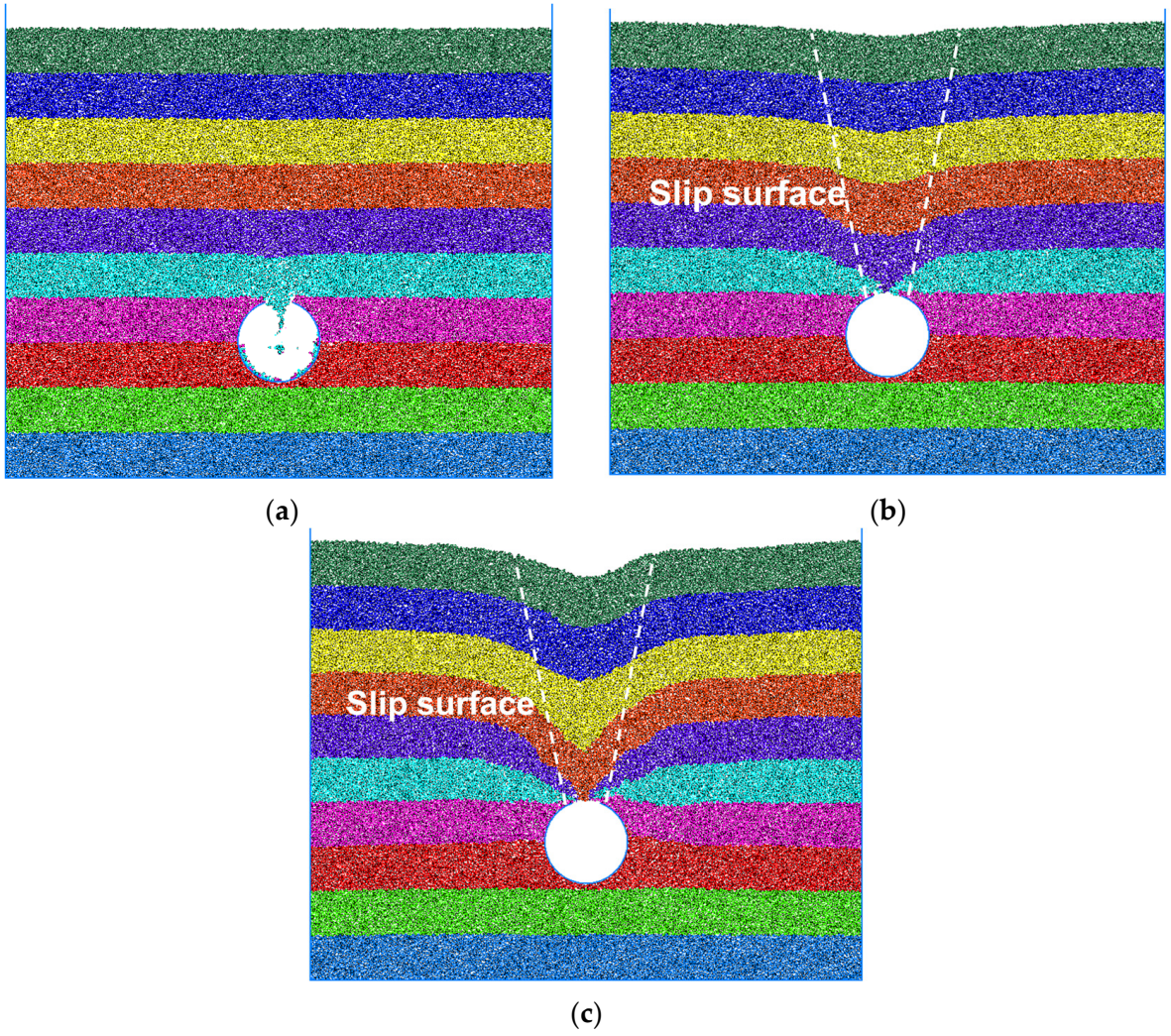

Figure 12. Simulation results of NSC soil: (**a**) tunnel leakage; (**b**) slip surfaces; (**c**) subsidence within the slip surfaces.

The numerical simulation results of the USC soil are shown in Figure 13. As can be seen from the figure, the numerical simulation reproduces the phenomena of seepage erosion induced by tunnel leakage and the development of unstable soil caves as observed in the tests. The strata surface remained stable during the development of seepage erosion.

The soil caves expanded upward with the development of seepage erosion and eventually induced the strata surface subsidence.

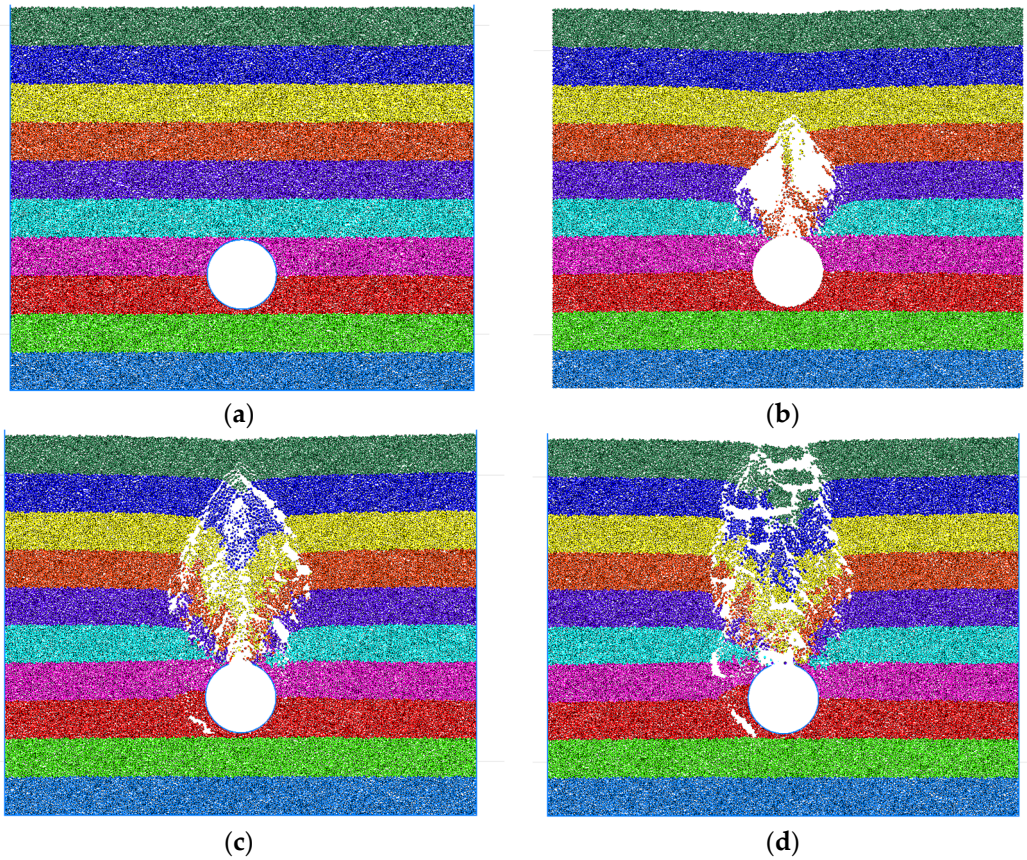

Figure 13. Simulation results of USC soil: (**a**) leakage at the tunnel top; (**b**) initial soil cave; (**c**) secondary soil cave; (**d**) surface subsidence.

The numerical simulated phenomena in the SSC strata are shown in Figure 14. It can be seen that the numerical simulation reproduced the phenomenon of stabilized soil cave in the SSC strata as observed in the model test, which appeared in the soil near the top of the tunnel after seepage occurred, but stabilized spontaneously with the continuation of seepage flow.

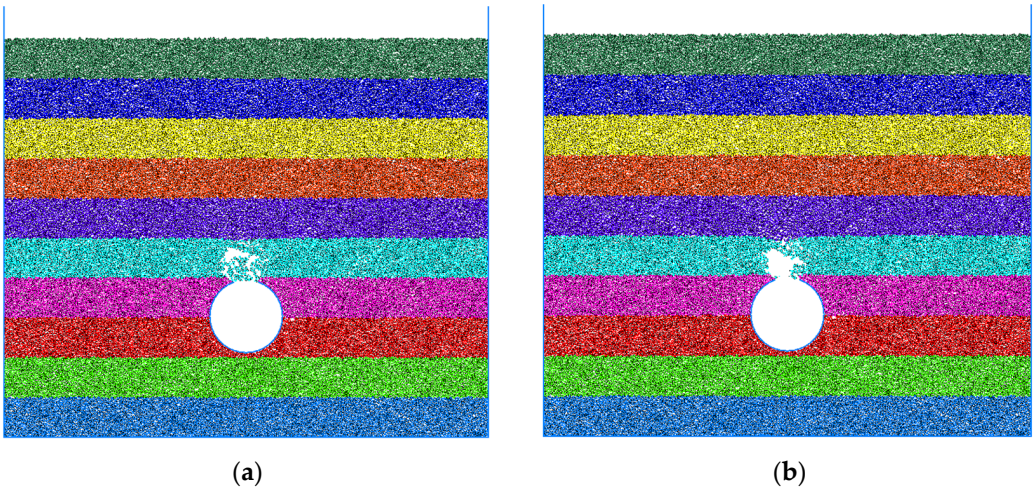

Figure 14. Simulation results of SSC soil: (**a**) initial soil cave at the tunnel top; (**b**) soil remains stable.

From the comparison between simulation results and the test results shown in Section 2.2, it can be seen that the numerical model can effectively reproduce the seepage erosion development characteristics of the four different soils. Therefore, the model can be further used to analyze the key factors in the seepage erosion process induced by tunnel leakage in different strata.

4. Seepage Erosion around Tunnel in Different Strata

4.1. Seepage Erosion Progression

To analyze the microscopic differences of seepage erosion occurring in the three types of soil, the changes in porosity of the three different soils were compared. It should be noted that the porosity of the assigned area was calculated by arranging a measuring circle at a fixed position and counting the volume of the pores inside the measuring circle. Therefore, when a little settlement occurs on the strata surface, a significant increase in porosity will occur due to the fixed position of the measuring circle, which is caused by the measurement error.

The distribution of porosity in the NSC soil after tunnel leakage was calculated, and is plotted in Figure 15. It can be seen that after the leakage of the tunnel starts, the porosity of the strata near the top of the tunnel and strata surface increases, as shown in Figure 15a. This indicates that after the leakage, seepage erosion occurred near the leakage point, and led to the strata surface settlement without the support of an arch. As the leakage continued, the porosity of the soil in the range from the top of the tunnel to the surface increased significantly, indicating that seepage erosion and loss of fine particles occurred in this area. At the same time, the ground surface showed obvious settlement, as shown in Figure 15b.

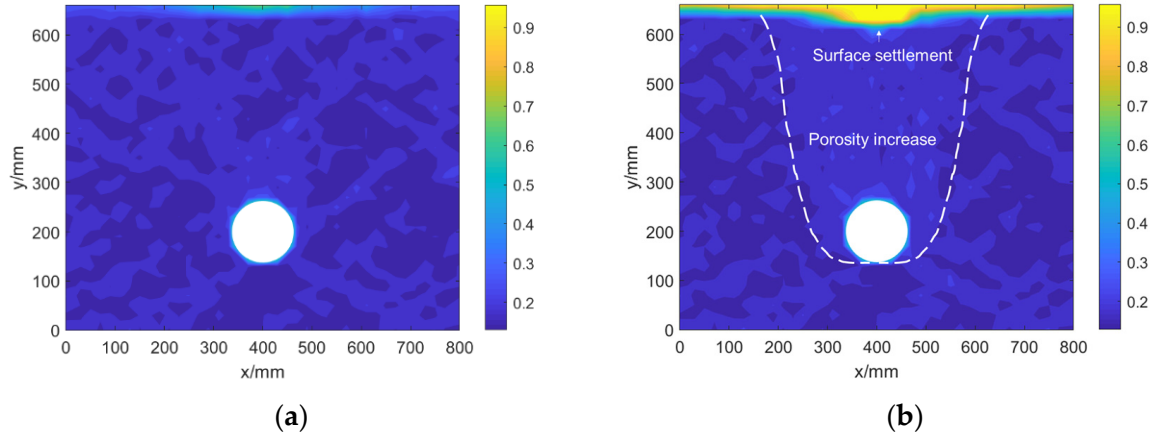

Figure 15. Porosity changes of NSC soil: (**a**) leakage starts; (**b**) surface settlement and porosity increase.

The distribution of porosity after the tunnel leakage in the USC soil is shown in Figure 16. It can be seen that (1) when the tunnel starts to leak, the porosity near the opening at the top of the tunnel increases rapidly, which also leads to a subsequent increase in the seepage rate and an accelerated erosion process, as shown in Figure 16a. (2) After the soil cave was formed at the top of the tunnel, the porosity of the strata inside the cave increased rapidly due to particle loss, as shown in Figure 16b,c. (3) When the soil surface subsided, a region of sharp increase in porosity was formed from the surface to the leakage point, as shown in Figure 16d. It can be further analyzed that after the tunnel leakage, the change of porosity is confined to the interior of the soil cave, and the porosity of the stratum outside the soil cave remains almost unchanged. This suggests that the soil cave hinders the loss of particles and causes seepage erosion to occur within the range of the soil cave.

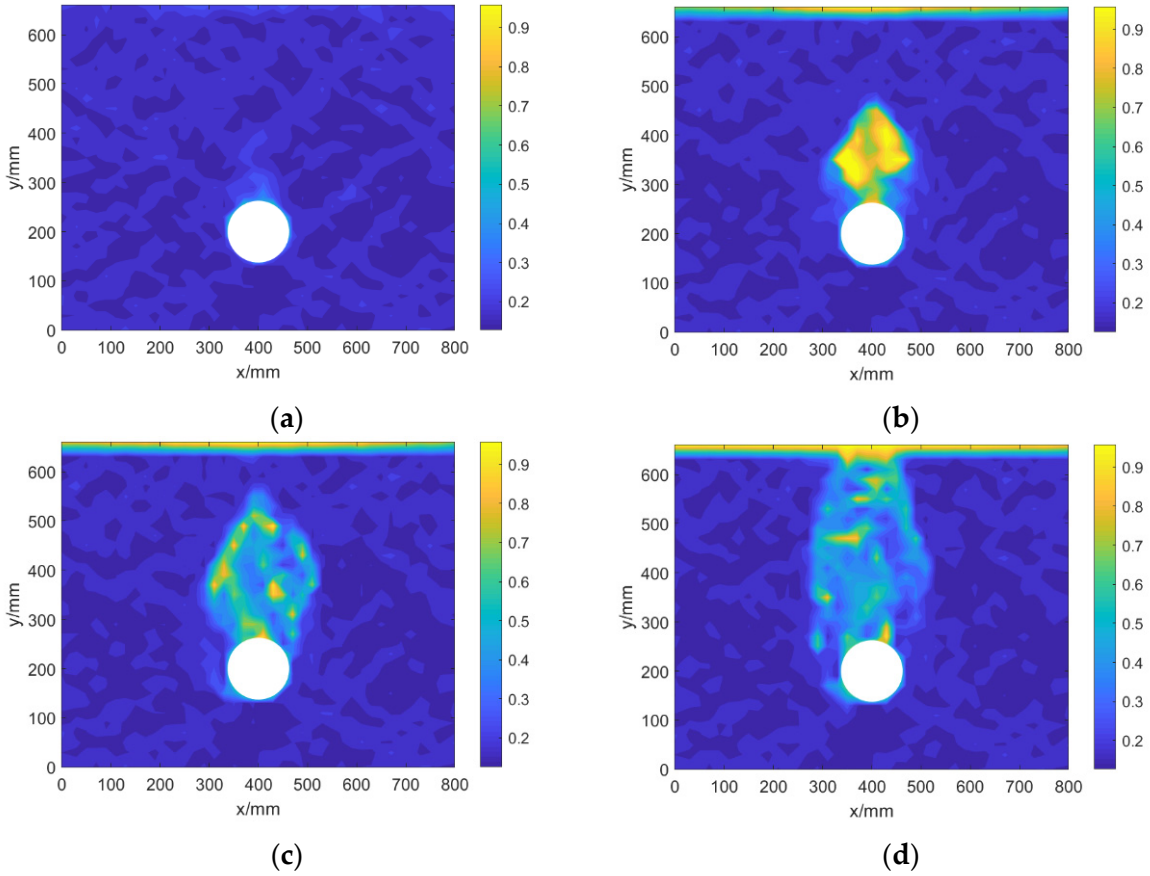

Figure 16. Porosity changes of USC soil: (**a**) leakage at the tunnel top; (**b**) initial soil cave; (**c**) secondary soil cave; (**d**) surface subsidence.

The distribution of porosity in the SSC soil was analyzed, and the distribution of porosity is shown in Figure 17. It can be seen that when the tunnel leakage occurred, the porosity near the opening at the top of the tunnel increased rapidly. After the initial soil cave was formed, the range of porosity change outside the opening remained stable after 16 million steps, indicating that the soil body was stable.

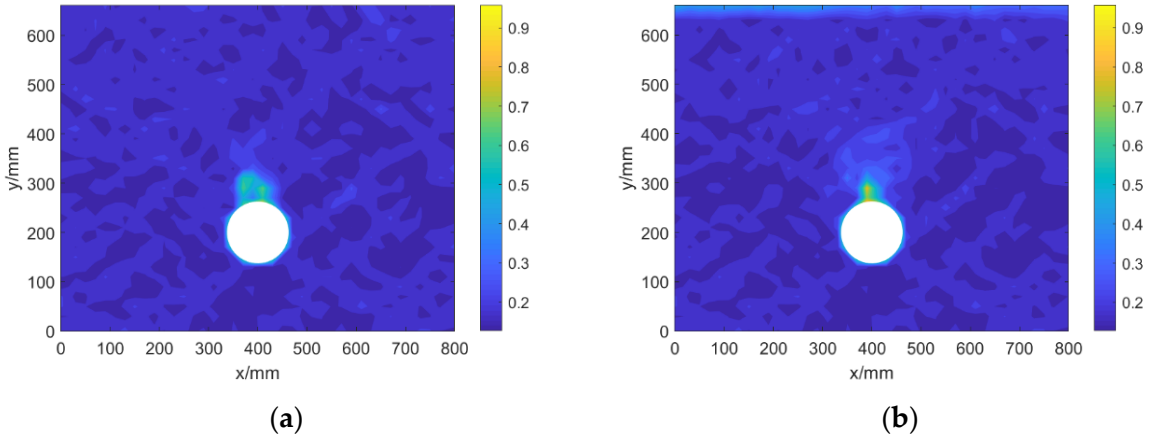

Figure 17. Porosity changes of SSC soil: (**a**) initial soil cave; (**b**) porosity after 16 million steps.

A comparison of the porosity changes induced by tunnel leakage in the three types of soil shows that (1) the seepage erosion area in NSC soils extended from the tunnel leakage point to the strata surface, with the largest area; (2) the seepage erosion in USC soils was

confined to the inner range of the soil caves, and the existence of the soil caves prevented the erosion of the surrounding soil; and (3) a stable initial soil cave formed in SSC soils, which confined the erosion area to the area near the tunnel leakage point.

4.2. Soil Displacement

Based on the simulation results, the displacement of different strata during seepage erosion was further compared numerically. To analyze the overall displacement characteristics of the strata after the tunnel leakage, four layers of monitoring points were set up above the tunnel at intervals of 100 mm from 0 mm (i.e., the top of the tunnel) to 400 mm (i.e., the strata surface). A total of 40 monitoring points were placed at intervals of 20 mm in the horizontal direction for each layer. It has to be noted that the monitoring point dropping to a height of 0 mm indicates the complete loss of water.

In the NSC soil, the distribution of displacements of the strata above the tunnel is shown in Figure 18. From the figure, it can be seen that after the tunnel leakage started, the top of the tunnel (i.e., layer 0 mm) first subsided, and, at the same time, the layer at a height of 100 mm also started to subside. With the continuation of particle loss, the strata at different heights above the top of the tunnel including the strata surface all began to subside.

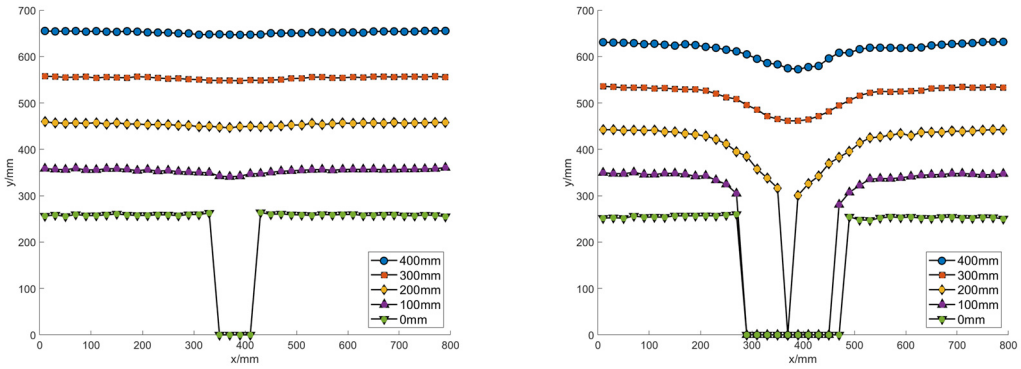

Figure 18. Displacement of soil NSC: (**a**) start of leakage; (**b**) subsidence of all layers.

The settlement of the strata after tunnel leakage-induced erosion in the USC strata is shown in Figure 19. From the figure, it can be seen that (1) after the leakage started, the layer at 0 mm was the first to subside at the location corresponding to the tunnel opening, but the layers at other heights remained stable. (2) After the formation of the initial soil cave, the particles above the tunnel at the heights of 0 to 200 mm all settled, but the heights of 300 mm and 400 mm remained stable. (3) After the formation of the secondary soil cave, the strata at the height of 0 mm to 300 mm above the tunnel all settle down obviously, but the surface remains stable. (4) After the destabilization of the secondary soil cave, the surface of the strata began to settle downward.

The displacement of the strata after tunnel leakage and erosion in the SSC formation is shown in Figure 20. From the figure, it can be seen that after the leakage started, the layer at 0 mm settled down first at the tunnel opening position, but the other layers above it remained stable. After 16 million steps of the calculation, the particles at 100 mm above the tunnel settle slightly, but remain stable overall, indicating that the strata stabilized spontaneously.

Comparison of the subsidence patterns of the strata shows the following differences between different soil types: (1) in the NSC stratum, the subsidence after the tunnel leakage was rapidly transferred to the surface, which was observed as overall subsidence from the top of the tunnel to the surface; (2) in the USC stratum, the soil lost after the tunnel leakage but the strata above the soil cave were temporarily stabilized due to the support of the

soil cave; (3) in the SSC stratum, the strata above the tunnel leakage were spontaneously stabilized after the tunnel leakage.

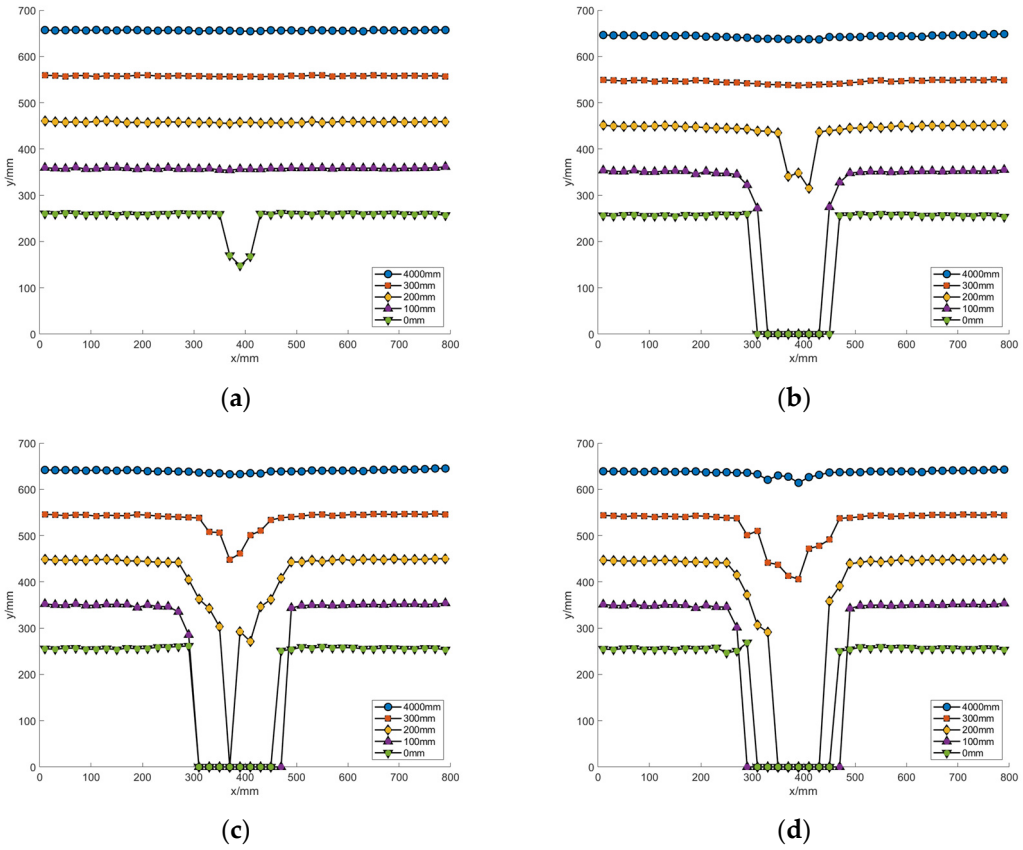

Figure 19. Displacement of soil USC: (**a**) leakage at the tunnel top; (**b**) initial soil cave; (**c**) secondary soil cave; (**d**) surface subsidence.

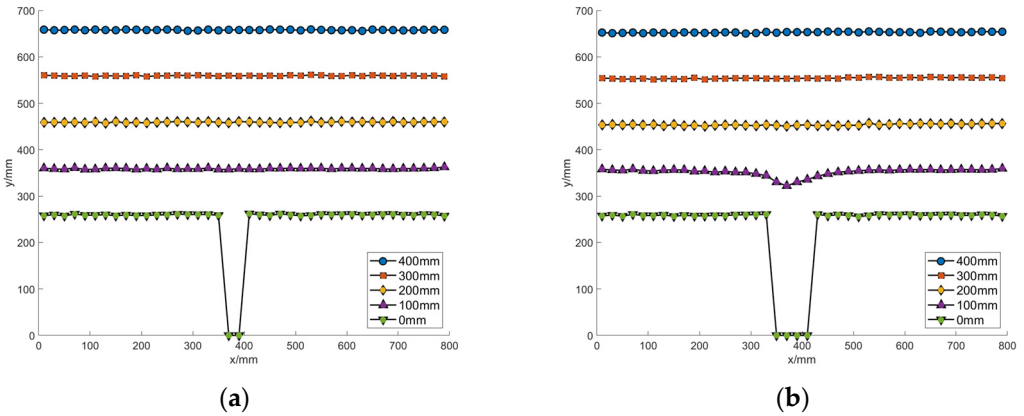

Figure 20. Displacement of soil SSC: (**a**) initial soil cave; (**b**) displacement after 16 million steps.

4.3. Soil Arching Effect

The macroscopic differences exhibited by the strata of the three different erosion modes essentially originate from the different stability behavior of soil arches, so the soil arching effect during the erosion of the three soils was analyzed based on numerical simulations. This soil arching effect is reflected by the contact force chain between particles in the simulation, in which the width of the contact force chain indicates the magnitude of the contact force.

The contact force chain in the NSC strata is shown in Figure 21. From the figure, it can be found that the tunnel leakage process is accompanied by the following changes in the soil arching effect: (1) Before the tunnel leakage starts, the contact force distribution shows a trend of large contact force at the bottom and small contact force at the top, because of the larger vertical stress in the soil at the bottom, as shown in Figure 21a. (2) After the leakage occurred at the top of the tunnel, the contact force chain of the soil above the leakage point formed an obvious soil arch state, as shown in Figure 21b. (3) As the leakage continued to develop, the stress arch was generated at a higher and wider extent, as shown in Figure 21c.

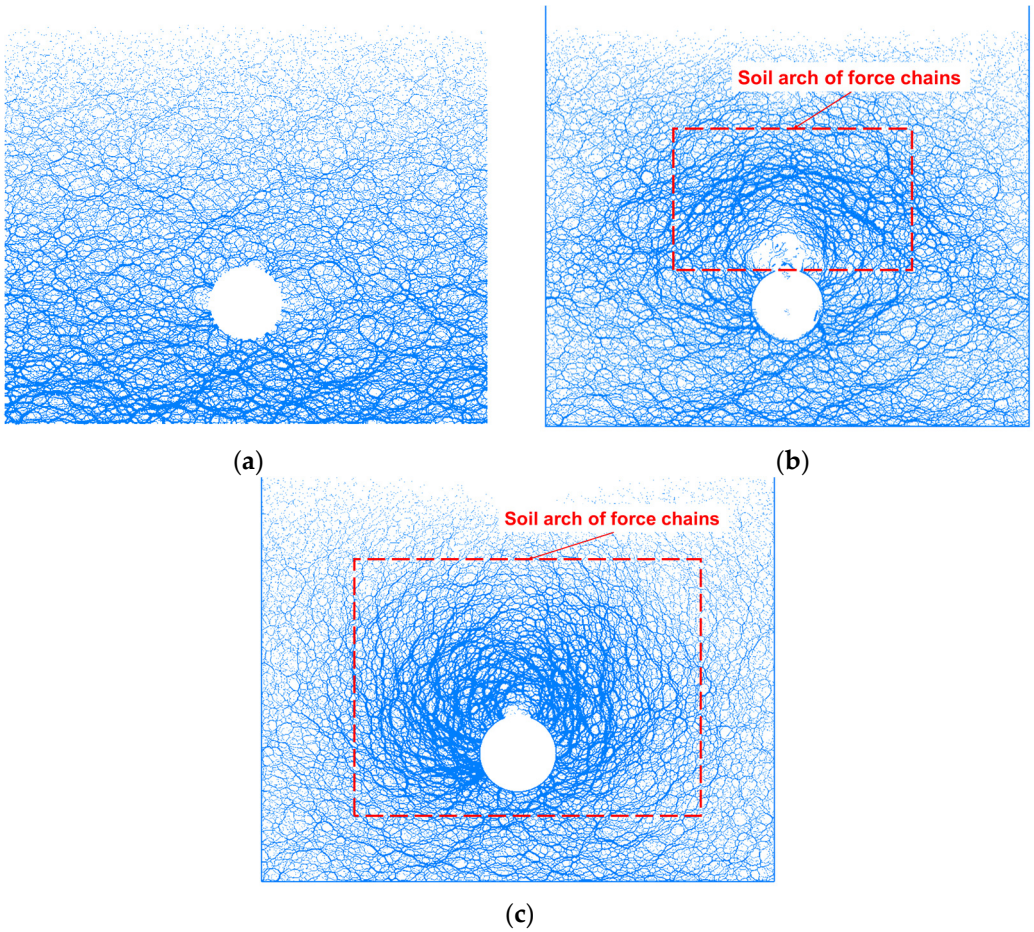

Figure 21. Contact force chain of NSC soil: (**a**) initial contact stress; (**b**) soil arching effect after leakage; (**c**) soil arch extension.

The changes in the contact force chain during seepage erosion of USC soil are shown in Figure 22. From the figure, it can be seen that the contact force chain exhibits the following changes, along with seepage erosion: (1) After the leakage occurred at the top of the tunnel, the contact force chain of the soil above the leakage point of the tunnel showed obvious soil arching, as shown in Figure 22 b, which indicated that the soil arching effect started to play a role after the leakage. (2) As the leakage continued to develop, the stress arch destabilized, and then arches were generated again in a higher and wider range, as shown in Figure 22c,d. (3) When the soil arch developed to a critical height, the soil arch destabilized completely, and there was no obvious contact force chain above the tunnel, while the surface soil particles subsided, as shown in Figure 22e.

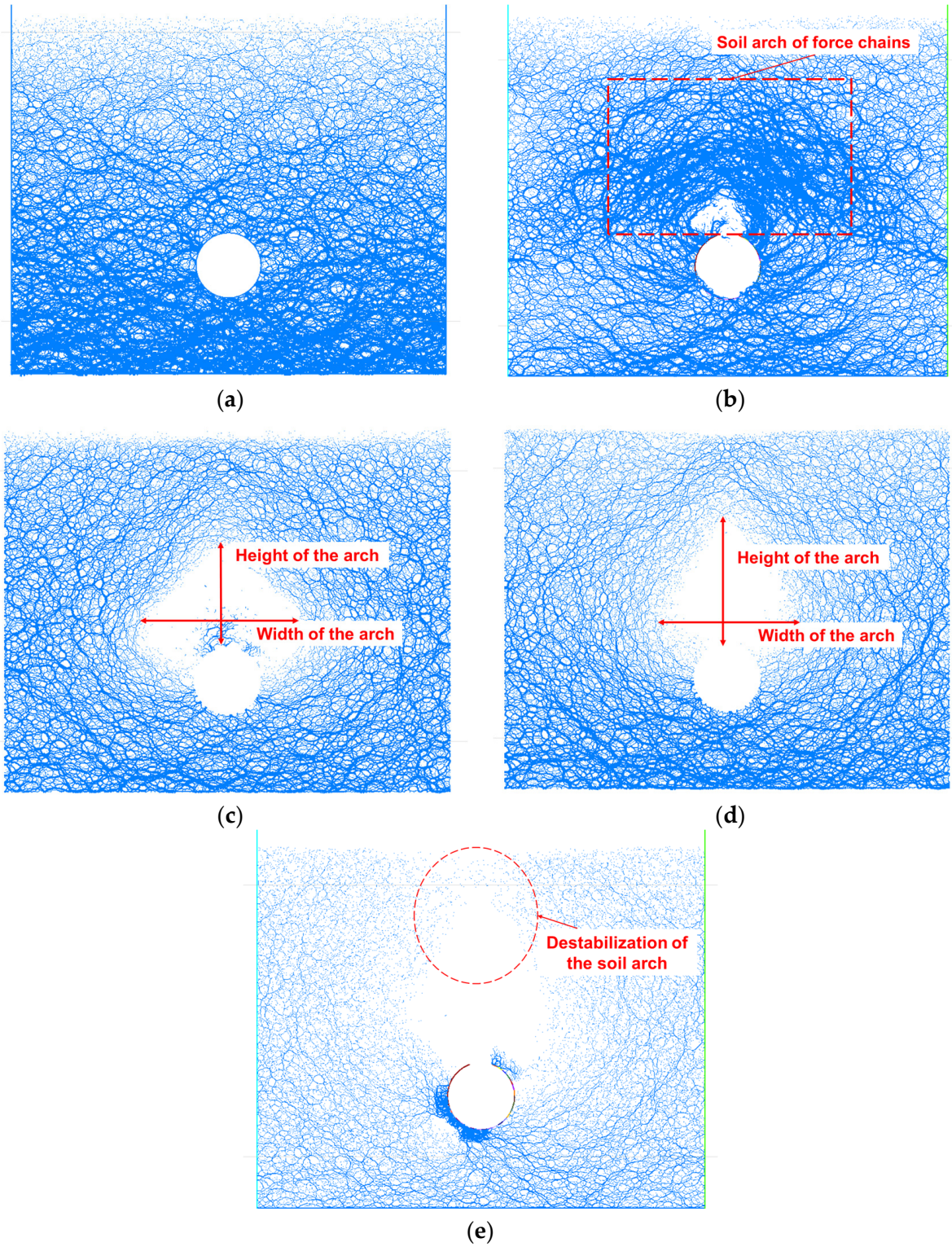

Figure 22. Contact force chain of USC soil: (**a**) initial contact force chain; (**b**) soil arch generation; (**c**) reappearance of the soil arch after destabilization; (**d**) upward development of the soil arch; (**e**) soil arch destabilization.

The change of the contact force chain between soil particles during seepage erosion in SSC soil is shown in Figure 23. From the figure, it can be found that after the leakage occurred at the top of the tunnel, the contact force chain of the soil above the tunnel

leakage point forms an obvious soil arch, as shown in Figure 23a. After 16 million steps of calculation, the soil arching effect at the top of the tunnel remained stable.

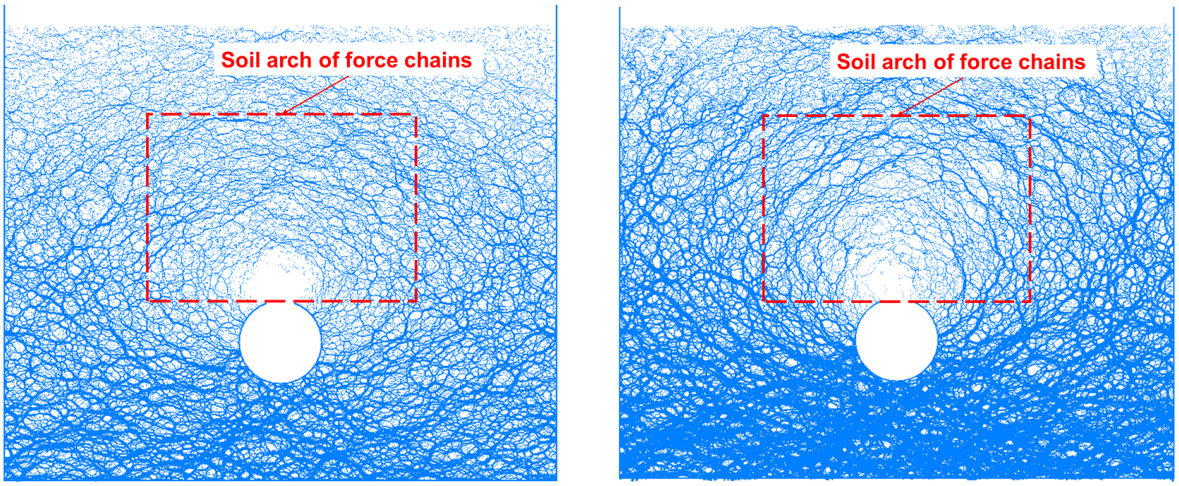

Figure 23. Contact force chain of SSC soil: (**a**) soil arch generation; (**b**) contact force chain after 16 million steps.

It can be found by observing the change of the soil arching effect in different strata that the macroscopic difference in soil cave stability originates from the strength of the soil arching effect. Although the soil cave phenomenon cannot be observed in the NSC stratum, the soil arching effect still exists. However, the soil arching effect of the NSC soil is not strong enough to prevent the loss of the soil particles. In the SSC stratum, the soil arching effect is strong and prevents seepage erosion from continuing, leading to spontaneous stabilization. In the USC stratum, the soil arching effect is somewhere in between, temporarily stabilizing and generating soil caves, but then destabilizing under continuous seepage force, leading to an upward progression of the eroded area.

5. Conclusions

This study diverges from past research on seepage erosion in underground structures that predominantly focused on sand strata. Instead, the research extends to various strata, presenting three types of erosion modes for the first time through a combination of experimental and simulation methods. Additionally, consideration for clay seepage erosion degradation was introduced into the coupled fluid–solid model, thus surpassing the limitations of previous studies that predominantly focused on simulating sand soil. This approach enabled the successful application of the method to the numerical simulation of multiple different strata, revealing three distinct erosion failure modes for the first time. The following conclusions were drawn from this study:

(1) Based on the differences in the seepage erosion modes after tunnel leakage, the soil can be classified into three categories: no soil cave (NSC), unstable soil cave (USC), and stable soil cave (SSC).

(2) The macroscopic phenomena of the three erosion modes are different: In NSC strata, there is no obvious soil cave phenomenon in the process of seepage erosion, and the multi-layer strata settle synchronously; in USC strata, there are unstable soil caves formed along with the erosion, and there is almost no deformation above the soil cave until the strata surface subside; in SSC strata, the soil stabilizes spontaneously and there is almost no settlement of the strata above the leakage point.

(3) The coupled fluid–solid numerical model, which considers the degradation of clay, can effectively simulate the development process of soils with different seepage erosion modes. The DEM-based fluid–solid coupling model can be used to analyze the particle–

water interaction phenomenon in the process of soil seepage erosion; the introduction of the clay degradation design can further solve the problem that the clay particles are too small to be simulated, and, at the same time, it can reflect the influence of clay particle loss.

(4) The difference between the three seepage erosion modes comes from the strength of the soil arching effect: the soil arch of the NSC strata is weak, which cannot prevent the development of seepage erosion, so the seepage erosion range is large, there is no soil cave observed, and the strata show overall settlement; the soil arch of the USC strata is stronger than that of the NSC strata, which limit the seepage erosion to the inner area of the soil arch, and the strata over the arch are temporarily stable, but in the continued action of the seepage force, the soil arch destabilizes and reappears until strata surface subside; SSC strata form the strongest soil arch, which prevents the seepage erosion, and leads to stabilization of the strata above the arch.

For ground subsidence accidents caused by tunnel leakage, different damage modes were observed in different strata. This study explored the causes and mechanisms of different erosion modes caused by tunnel leakage in different strata and enhanced the understanding of the relationship between strata and erosion modes. At the same time, the research provided practical insights and tools for engineers to effectively manage and prevent the associated risks in infrastructure projects.

However, certain limitations in this study are acknowledged. The use of two-dimensional numerical simulations represents a constraint, and the potential for further advancements is recognized. In future research endeavors, the incorporation of three-dimensional numerical simulations is aimed at enhancing the accuracy and comprehensiveness of the findings. These future research directions will contribute to refining the understanding of seepage erosion in underground engineering and improving the predictive capabilities of the models under diverse geological conditions.

Author Contributions: Conceptualization and methodology, Q.S. and X.L.; validation, formal analysis, investigation, and writing—original draft preparation, Q.S.; writing—review and editing and supervision, X.L., W.D.C. and L.T.; project administration and funding acquisition, X.L. All authors have read and agreed to the published version of the manuscript.

Funding: This research was funded by the National Natural Science Foundation of China, grant number 52078376.

Institutional Review Board Statement: Not applicable.

Informed Consent Statement: Not applicable.

Data Availability Statement: The original contributions presented in the study are included in the article, further inquiries can be directed to the corresponding author.

Acknowledgments: The first author would like to express his appreciation for the scholarship from the China Scholarship Council (No. 202106260163) for his study at Ghent University.

Conflicts of Interest: The authors declare no conflicts of interest.

References

1. Fang, Q.; Zhang, D.; Wong, L. Shallow tunnelling method (STM) for subway station construction in soft ground. *Tunn. Undergr. Space Technol. Inc. Trenchless Technol. Res.* **2012**, *29*, 10–30. [CrossRef]
2. Zucca, M.; Crespi, P.; Tropeano, G.; Erbì, E. 2D equivalent linear analysis for the seismic vulnerability evaluation of multi–propped retaining structures. In Proceedings of the XVII ECSMGE-2019, Reykjavík, Iceland, 1–6 September 2019.
3. Zucca, M.; Valente, M. On the limitations of decoupled approach for the seismic behaviour evaluation of shallow multi-propped underground structures embedded in granular soils. *Eng. Struct.* **2020**, *211*, 110497. [CrossRef]
4. Ni, J.C.; Cheng, W.-C. Characterising the failure pattern of a station box of Taipei Rapid Transit System (TRTS) and its rehabilitation. *Tunn. Undergr. Space Technol.* **2012**, *32*, 260–272. [CrossRef]
5. Sato, M.; Kuwano, R. Influence of location of subsurface structures on development of underground cavities induced by internal erosion. *Soils Found.* **2015**, *55*, 829–840. [CrossRef]
6. Chai, J.; Shen, J.S.; Yuan, D.-J. Mechanism of tunneling-induced cave-in of a busy road in Fukuoka city, Japan. *Undergr. Space* **2018**, *3*, 140–149. [CrossRef]

7. Korff, M.; Mair, R.J.; Van Tol, A.F.; Kaalberg, F. Building damage and repair due to leakage in a deep excavation. *Proc. Inst. Civ. Eng.-Forensic Eng.* **2011**, *164*, 165–177. [CrossRef]
8. Rosso, M.; Marasco, G.; Tanzi, L.; Aiello, S.; Aloisio, A.; Cucuzza, R.; Chiaia, B.; Cirrincione, G.; Marano, G. In Advanced deep learning comparisons for non-invasive tunnel lining assessment from ground penetrating radar profiles. In Proceedings of the ECCOMAS Congress 2022—8th European Congress on Computational Methods in Applied Sciences and Engineering, Oslo, Norway, 5–9 June 2022.
9. Domaneschi, M.; Cucuzza, R. Structural Resilience through Structural Health Monitoring: A Critical Review. In *Data Driven Methods for Civil Structural Health Monitoring and Resilience*; CRC Press: Boca Raton, FL, USA, 2024; pp. 1–13.
10. Domaneschi, M.; Cucuzza, R.; Martinelli, L.; Noori, M.; Marano, G.C. A probabilistic framework for the resilience assessment of transport infrastructure systems via structural health monitoring and control based on a cost function approach. *Struct. Infrastruct. Eng.* **2024**, 1–13. [CrossRef]
11. Zheng, G.; Dai, X.; Diao, Y.; Zeng, C.-F. Experimental and simplified model study of the development of ground settlement under hazards induced by loss of groundwater and sand. *Nat. Hazards* **2016**, *82*, 1869–1893. [CrossRef]
12. Guo, S.; Shao, Y.; Zhang, T.; Zhu, D.Z.; Zhang, Y. Physical modeling on sand erosion around defective sewer pipes under the influence of groundwater. *J. Hydraul. Eng.* **2013**, *139*, 1247–1257. [CrossRef]
13. Tang, Y.; Zhu, D.Z.; Chan, D.H. Experimental study on submerged sand erosion through a slot on a defective pipe. *J. Hydraul. Eng.* **2017**, *143*, 04017026. [CrossRef]
14. Zhang, P.; Mu, L.; Huang, M. A coupled CFD-DEM investigation into hydro-mechanical behaviour of gap-graded soil experiencing seepage erosion considering cyclic hydraulic loading. *J. Hydrol.* **2023**, *624*, 129908. [CrossRef]
15. Long, Y.-Y.; Tan, Y. Soil arching due to leaking of tunnel buried in water-rich sand. *Tunn. Undergr. Space Technol.* **2020**, *95*, 103158. [CrossRef]
16. Zhang, Z.; Mao, M.; Pan, Y.; Zhang, M.; Ma, S.; Cheng, Z.; Wu, Z. Experimental study for joint leakage process of tunnel lining and particle flow numerical simulation. *Eng. Fail. Anal.* **2022**, *138*, 106348. [CrossRef]
17. Liu, X.; Chen, C.; Yu, Q.; Xia, K.; Liu, X.; Wang, Y. Experimental study on the influence of clay particle contents on the stability of soil caves. *Chin. J. Rock Mech. Eng.* **2021**, *40*, 1914–1922. (In Chinese)
18. Thielicke, W.; Sonntag, R. Particle Image Velocimetry for MATLAB: Accuracy and enhanced algorithms in PIVlab. *J. Open Res. Softw.* **2021**, *9*, 12. [CrossRef]
19. Kodieh, A.; Gelet, R.; Marot, D.; Fino, A. A study of suffusion kinetics inspired from experimental data: Comparison of three different approaches. *Acta Geotech.* **2021**, *16*, 347–365. [CrossRef]
20. Ahmadi, M.; Shire, T.; Mehdizadeh, A.; Disfani, M. DEM modelling to assess internal stability of gap-graded assemblies of spherical particles under various relative densities, fine contents and gap ratios. *Comput. Geotech.* **2020**, *126*, 103710. [CrossRef]
21. Wautier, A.; Bonelli, S.; Nicot, F. Scale separation between grain detachment and grain transport in granular media subjected to an internal flow. *Granul. Matter* **2017**, *19*, 22. [CrossRef]
22. Abdou, H.; Emeriault, F.; Plé, O. New approach to describe hydro-mechanical phenomenon of suffusion: Erosion, transport and deposition. *Eur. J. Environ. Civ. Eng.* **2020**, *24*, 2342–2360. [CrossRef]
23. Yang, J.; Yin, Z.-Y.; Laouafa, F.; Hicher, P.-Y. Modeling coupled erosion and filtration of fine particles in granular media. *Acta Geotech.* **2019**, *14*, 1615–1627. [CrossRef]
24. Zhu, H.P.; Zhou, Z.Y.; Yang, R.; Yu, A. Discrete particle simulation of particulate systems: Theoretical developments. *Chem. Eng. Sci.* **2007**, *62*, 3378–3396. [CrossRef]
25. Carman, P.C. Flow of gases through porous media. *Butterworths Sci. Publ.* **1956**, *45*, 2145–2152.
26. Itasca. *Particle Flow Code in 2 Dimensions Online Manual*, Version 5.0; Itasca Consulting Group Incorporated: Minneapolis, MN, USA, 2015.
27. Itasca, F. *Fast Lagrangian Analysis of Continua in 3-Dimension (FLAC3D V 5.01)*; Itasca Consulting Group: Minneapolis, MN, USA, 2012.
28. Anderson, J.D.; Wendt, J. *Computational Fluid Dynamics*; Springer: Berlin/Heidelberg, Germany, 1995; Volume 206.
29. Gu, D.; Liu, H.; Huang, D.; Zhang, W.; Gao, X. Development of a modeling method and parametric study of seepage-induced erosion in clayey gravel. *Int. J. Geomech.* **2020**, *20*, 04020219. [CrossRef]
30. Gu, D.M.; Huang, D.; Liu, H.L.; Zhang, W.G.; Gao, X.C. A DEM-based approach for modeling the evolution process of seepage-induced erosion in clayey sand. *Acta Geotech.* **2019**, *14*, 1629–1641. [CrossRef]
31. Hanson, G.; Cook, K.; Simon, A. Determining erosion resistance of cohesive materials. In Proceedings of the American Society of Civil Engineers Water Resources Conference, Seattle, WA, USA, 1 August 1999.
32. Deisman, N.; Mas Ivars, D.; Pierce, M. PFC2D Smooth joint contact model numerical experiments. In Proceedings of the GeoEdmonton, Edmonton, AB, Canada, 21–24 September 2008.
33. Tsuji, Y.; Kawaguchi, T.; Tanaka, T. Discrete particle simulation of two-dimensional fluidized bed. *Powder Technol.* **1993**, *77*, 79–87. [CrossRef]

Disclaimer/Publisher's Note: The statements, opinions and data contained in all publications are solely those of the individual author(s) and contributor(s) and not of MDPI and/or the editor(s). MDPI and/or the editor(s) disclaim responsibility for any injury to people or property resulting from any ideas, methods, instructions or products referred to in the content.